ELSEVIER

Chemical Engineering Journal 74 (1999) 117–127

Chemical Engineering Journal

Structural and rheological properties of *n*-decane confined between graphite surfaces

Ramkumar Balasundaram[a], Shaoyi Jiang[a,*], James Belak[b]

[a]*Department of Chemical Engineering, Kansas State University, Manhattan, KS 66056, USA*

[b]*Condensed Matter Physics Division, Lawrence Livermore National Laboratory, University of California, Livermore, CA 94551, USA*

Abstract

We report a constant-volume and constant-pressure molecular dynamics study of the fluid structure, flow boundary condition, and shear viscosity of *n*-decane confined between graphite surfaces under various shear rates at 480 K using an anisotropic united atom model. The effect of surface corrugation, wall–fluid interaction strength, and load on these properties is investigated in this work. Our results show that the surface corrugation has a pronounced effect on rheological properties, but not on structural and orientational properties at the temperature studied. The shear thinning behavior of the confined fluids is observed for all cases under the shear rates studied. Our results also show that the velocity profile deviates more from the perfect linear profile with increasing surface corrugation, wall–fluid interaction strength, shear rate, and normal load. Slip occurs throughout the range of parameters studied. The fluid layers near the walls could be locked to each other even though slip occurs at the solid–fluid interface. © 1999 Elsevier Science S.A. All rights reserved.

Keywords: Molecular dynamics; Confined fluid; Rheology

1. Introduction

An understanding of the atomic processes occurring at the interface of two dry or wet materials when they are brought together or moved with respect to one another is central to many technological problems, including adhesion, lubrication, friction, wear, wetting, and spreading [1–6]. The classical physics of the continuum has historically provided most of the theoretical and computational tools for engineering applications. However, technology is now reaching nano-scale dimensions where the approximations used in the continuum modeling are no longer valid. One of the fundamental assumptions in fluid mechanical formulations of Newtonian flow past solids is the continuity of the tangential component of velocity across a boundary known as the "no-slip" boundary condition (BC) [7]. However, recent microscopic experiments [8] and molecular dynamics (MD) simulations [9–11] indicate that the BC is different at the molecular level. Modern microscopic experimental techniques coupled with molecular simulation provide a unique understanding of these problems at the atomic scale. Measurements by the surface force apparatus (SFA) [8,12] and the quartz crystal microbalance (QCM) [13] have revealed much about boundary lubrication phenomena. Simulations of confined fluids under shear [14–39] have enhanced our understanding of these experiments.

It was shown in the SFA experiments [8,12] that the behavior of confined fluids at small plate separations is very different from that of bulk fluids. In the Newtonian regime, the effective viscosity is orders of magnitude larger than the shear viscosity of the bulk fluid. At higher shear rates, there is a transition to a non-Newtonian regime where the effective viscosity decreases with increasing shear rates for most cases according to a power law, $\eta_{\text{eff}} \sim \gamma^{\alpha}$. The value of α is found to be $-2/3$ for a number of fluids such as octamethlycyclotetrasioxane (OMCTS) and dodecane under high pressures [12,40] though the value of α may depend on the load and vary for other systems such as hexadecane [41]. Robbins and co-workers [16,17] carried out simulations with a bead-spring model (coarse-grained model) for linear-chain molecules of varying lengths to study the response under steady shear. The shear thinning behavior appears to follow a universal power law with $\alpha = -2/3$ near the glassy state for chain lengths between 4 and 12 and for various wall-strengths, loads, and numbers of fluid layers studied. Manias et al. [33,34] used the same bead-spring model in their simulations and analyzed viscosities inside the solid–fluid interface and the inner fluid film. They found that nearly all the shear thinning takes place inside the solid–oligomer interface and the shear thinning inside the inter-

---

[*] Corresponding author. E-mail: sjiang@pluto.cheme.ksu.edu

PII: S1385-8947(99)00063-7

facial area is determined by the wall affinity. While the loads used in the Manias' simulations are much smaller than the ones used in experiments [33,34], the loads used in the Robbins' simulations are quite high so that fluids are near the glassy state [16,17]. Thus, the difference between these two simulations could be due to different loads used in the simulations. In the recent simulations of confined fluids by Stevens et al. [37] using a realistic model (atomic-scale model), it was found that the value of α depends on the wall strength. The same conclusion was reached in the simulations by Khare et al. [35]. A direct comparison between simulations with an atomic-scale model and experiments is difficult due to the fact that the shear velocity in these simulations differs by orders of magnitude from that in experiments. It should be pointed out that the simulations with an atomic-scale model [37] and with a bead-spring model [16,17] are also different. In the simulations by Robbins and co-workers [16,17], the temperature T is $1.1\varepsilon/k$, and the Lennard-Jones (LJ) coupling strength is ε=0.91kT. These simulations were carried out near the glassy state where shear viscosity changes several orders of magnitude with small increases in shear rates. However, for hexadecane simulations by Stevens et al. [37], the LJ parameters, $\varepsilon_{\mathrm{CH}_2} = 0.15kT$ and $\varepsilon_{\mathrm{CH}_3} = 0.35kT$ (in units of temperature T=323 K), are much smaller. To simulate hexadecane at a temperature equivalent to the bead-spring system, one needs to go to the 50–100 K range where hexadecane crystallizes. It is well known that the viscosity increases as the temperature decreases. The bead-spring system is thus at a more viscous point. Lowering the temperature is equivalent to decreasing the critical shear rate. The temperature shift is equivalent to a shift of the time scale [37]. This explains why the bead-spring simulations can reproduce the SFA experiments in spite of the difference in shear velocity between simulations and experiments.

In this paper, we present the results of MD simulations of n-decane confined between graphite surfaces at 480 K using an anisotropic united atom model (AUA). The effect of wall–fluid strength, shear rate, and pore size on the flow boundary condition has been studied previously in details for spherical LJ systems confined between LJ walls [14,15,38]. Very few results are available on the velocity profile of confined chain molecules [25]. Furthermore, additional work is needed to resolve the discrepancies concerning the existence of a universal power law for describing the shear thinning behavior of confined fluids. For these reasons, the effect of surface corrugation and wall–fluid strength on the flow boundary condition and the shear thinning behavior of confined n-decane is investigated in this work. We chose n-decane because its chain length falls between 4 and 12 for which a universal power law with α=−2/3 from constant-pressure simulation and −1/2 from constant-volume simulations was found in the bead-spring simulations by Robbins and co-workers [16,17]. For the system of hexadecane studied by Stevens et al. [37], experiments found that α is somewhat less than 1/2 and depends on the load [41]. Simulations were carried out at 480 K, corresponding to the conditions to which organic fluids are typically exposed during engine lubrication. Since the temperature is well above its melting point of 243 K, this allows one to examine a wide range of loads while remaining in the stable region of the liquid phase. Graphite surface was used because it has been extensively studied [42].

2. Potential models and simulation methods

In applying a valence force field to long chain hydrocarbon molecules, there are essentially two models – the all atom and the united atom (UA) models [43]. While the all atom model is more accurate in principle, it is more computationally expensive. The UA model treats the hydrogen–carbon groups as pseudo-atoms and is about three times faster than the all atom model. Recently, an improvement over the UA model, the AUA model, has been proposed by Toxvaerd [44]. As in the UA model, the hydrogen–carbon group is also represented by a single interaction site. The interaction site is placed in the geometrical center of the group by displacing from the center of the carbon atom along the bisector of the HCH bond angle in the CCC plane while the mass of the group is placed on the carbon nucleus which is the moving center. The energy difference in the interaction between a pair of methylene-units in different relative orientations is accounted for in the AUA model. This energy difference is important, especially in dense systems. The AUA model does not extend the computer time significantly and requires only minor changes in a traditional MD program for the UA model. A more detailed description of the AUA model can be found in [44]. The bond stretching vibrational frequency is usually much higher than other intra-molecular vibrational modes and hence does not couple strongly with other modes. For these molecules, the constraint of constant bond length does not significantly affect the overall motion and results in a computational saving of a factor of three. Elimination of the bond length motion is accomplished by inserting a constraint force into the simulation. In this work, the AUA model with bond constraints is adopted. The bond angle potential is described by a cosine harmonic potential:

$$E_{\text{angle}} = 1/2\, k_\theta(\cos\theta_i - \cos\theta_0)^2. \tag{1}$$

The torsional potential [45] is described by

$$E_{\text{torsion}} = \sum_{m=0}^{5} V_m(\cos\phi)^m. \tag{2}$$

The valence parameters of the force field used are given in Table 1. The intra- and inter-molecular non-bonded interactions are described by the shifted-force potential [46] truncated at r_c=2.5σ_{ij}. They are calculated in the AUA fashion. The shifted-force potential is used to remove the discontinuities in the potential and force. The intra-molecular non-bonded interactions are not used between nearest

Table 1
Valence and van der Waals parameters of the force field used

Bond	R_0 (nm)[a]					
C–C	0.1545					
Angle (Eq. (1))	K_θ[b]	θ_0 (deg)				
C–C–C	520	114.6				
Torsion[c] (Eq. (2))	V_0	V_1	V_2	V_3	V_4	V_5
C–C–C–C	8.6279	20.1703	0.6788	−26.0183	−1.3575	−2.1012
VDW	σ (nm)	ε/k (K)	Mass (a.m.u.)	d (nm)[d]		
CH_3	0.3527	120.0	15.0	0.032		
CH_2	0.3527	80.0	14.0	0.032		

[a] Bond length is fixed at 0.1545 nm.

[b] Unit in (kJ/mol)/radian^2.

[c] Units in kJ/mol.

[d] d is the distance between the position of the interaction site and the carbon nucleus.

neighbors (1–2 interactions) and next nearest neighbors (1–3 interactions). The values of masses and LJ interaction parameters for different groups are given in Table 1. The parameters for the interactions between different groups are calculated with the Lorentz–Berthelot combination rule.

A solid–fluid model with laterally varying periodicity based on the usual Fourier expansion truncated after first order has been used [47,48]:

$$E_{\mathrm{sf}}(x,y,z) = E_{\mathrm{sf}}^{(0)}(z) + E_{\mathrm{sf}}^{(1)}(z)f(x,y), \tag{3}$$

where $E_{\mathrm{sf}}^{(0)}(z)$ is the 10–4–3 solid–fluid potential as given by

$$E_{\mathrm{sf}}^{(0)}(z) = A\left[\frac{2}{5}\left(\frac{\sigma_{\mathrm{sf}}}{z}\right)^{10} - \left(\frac{\sigma_{\mathrm{sf}}}{z}\right)^{4} - \left(\frac{\sigma_{\mathrm{sf}}^4}{3\Delta(0.61\Delta + z)^3}\right)\right], \tag{4}$$

where $A = 2\pi\rho_{\mathrm{s}}\varepsilon_{\mathrm{sf}}\sigma_{\mathrm{sf}}^2\Delta$, z is the distance between a fluid particle and the substrate surface, and ρ_{s} is the solid density. The graphite parameters are σ_{ss}=0.340 nm, $\varepsilon_{\mathrm{ss}}/k$=28.0 K, Δ=0.335 nm, and ρ_{ss}=114 nm^{-3} [47,48]. The structureless 10–4–3 potential is often used in adsorption studies, but is of limited use for the study of fluid flow since it cannot transfer tangential momentum and thus prevents the possibility of inducing a flow by moving the walls. The $E_{\mathrm{sf}}^{(1)}(z)$ is given by

$$E_{\mathrm{sf}}^{(1)}(z) = B\left[C\left(\frac{a_1}{z}\right)^5 K_5\left(\frac{4\pi z}{\sqrt{3}a_1}\right) - D\left(\frac{a_1}{z}\right)^2 K_2\left(\frac{4\pi z}{\sqrt{3}a_1}\right)\right], \tag{5}$$

with $B = 4\pi\varepsilon_{\mathrm{sf}}\sigma_{\mathrm{sf}}^6/\sqrt{3}a_1^6$, $C = \sigma_{\mathrm{sf}}^6/30a_1^6(2\pi/\sqrt{3})^5$, $D = 2(2\pi/\sqrt{3})^2$, and a_1=0.246 nm. K_2 and K_5 are modified Bessel function of the second kind. For the graphite basal plane, the laterally periodic function $f(x,y)$ is

$$f(x,y) = -2\left[\cos 2\pi\left(\frac{x}{a_1} + \frac{y}{\sqrt{3}a_1}\right) + \cos 2\pi\left(\frac{x}{a_1} - \frac{y}{\sqrt{3}a_1}\right) + \cos\frac{4\pi y}{\sqrt{3}a_1}\right]. \tag{6}$$

The above potential neglects a number of effects, such as anisotropic polarizability of the surface atoms, three body terms, substrate mediated dispersion energy, and so forth. For this reason we have considered a modified form of the truncated Fourier expansion [42], namely,

$$E_{\mathrm{sf}}(x,y,z) = E_{\mathrm{sf}}^{(0)}(z) + \lambda E_{\mathrm{sf}}^{(1)}(z)f(x,y), \tag{7}$$

where λ is a parameter that enables the corrugation of the wall potential to be varied. The site-solid potential energies for an interaction site at different positions over the graphite basal plane are given in Fig. 1(a) for different values of λ. The effect of λ on the flow boundary condition and shear viscosity is studied in this work. In our simulations, the surface was built from a unit cell, which contains six hexagon sites as shown in Fig. 1(b) in such a way as to meet the requirement that the periodic boundary conditions must match the symmetry of the external field. A similar surface was used in the studies of the commensurate–incommensurate transition of methane adsorbed on graphite at low temperatures [42] and the melting of nitrogen on graphite [49]. The simulation surface was constructed from a 8×4 array of unit cells, giving it a dimension of 3.408×2.951 nm. The system consists of 64 *n*-decane molecules.

Thin films under shear are studied with MD methods by modeling two surfaces with small separation and a confined film within. Periodic boundary conditions are used within the plane of the film. Shear is imposed by sliding the two walls relative to each other at velocities U and $-U$ for the top and bottom plates, respectively, while controlling the system temperature and wall separation (or load). When a fluid is under an applied shear, work done on the system is converted into heat. Appropriate coupling to a thermal reservoir (thermostat) is needed to remove the heat. Precaution must be taken to avoid biasing the flow and altering simulated properties. It was previously shown that an inappropriate thermostat can bias the flow [10,51]. Two

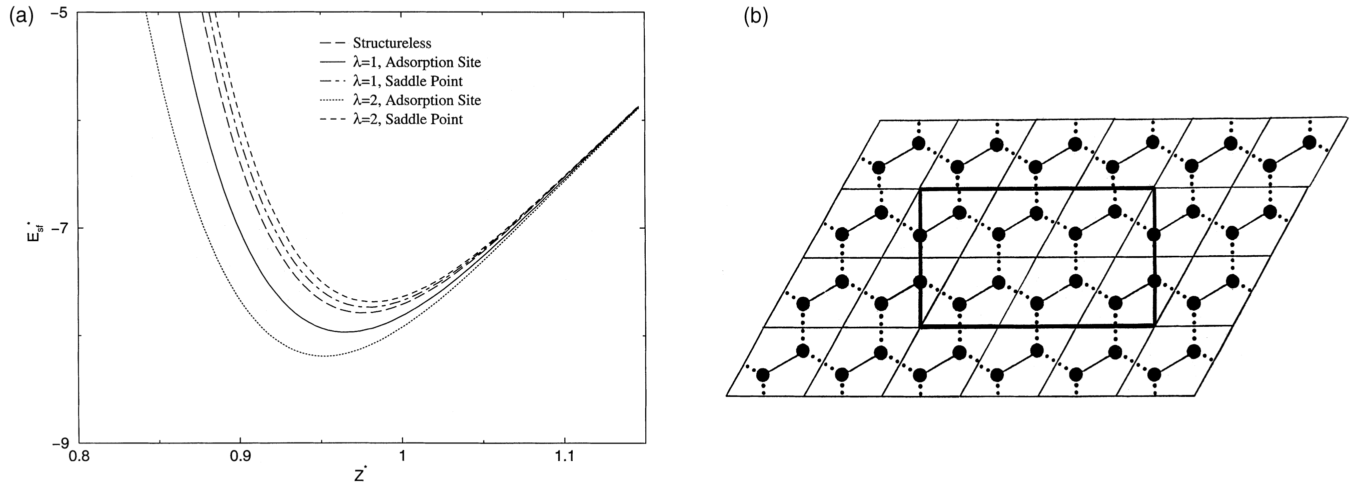

Fig. 1. (a) The site-solid potential curves for a CH_2 interaction site at the adsorption site and saddle point over the graphite basal plane, and (b) the graphite surface. The unit cell of the graphite lattice is indicated by the bold line and the solid points denote the carbon atoms.

approaches for shear flow simulations could be used: in one case, the sheared fluid is not thermostated and only the confining walls are maintained at a constant temperature, while in the other, a thermostat is employed to keep the entire mass of the sheared fluid at a constant temperature. Khare et al. [36] recently showed that in the first case the sheared fluid undergoes significant viscous heating at the shear rates studied, consistent with experimental observations. It was shown [36] that the results for transport coefficients are significantly affected by the thermostat. The viscous heat produced in our simulations is not as significant as that in the work by Khare et al. [36] where the temperature in the middle of the pore could be 6–7 times higher than that of the walls. Our results show that temperature profiles are constant across the gap for all the cases studied except for the case where the wall energy parameter was changed to ε_{ff}/k=1000 K. In this case, the temperature in the middle of the pore reaches 4.85 as compared to the target temperature of T^*=4.0. This is mainly due to the small pore size (H^*=8.0) studied here as compared to H^*=18.0 used in the work by Khare et al. [36]. Furthermore, our results show that when the viscous heat produced is not very large, velocity profiles and shear viscosities obtained with the two thermostating methods are basically the same. Similar behavior was found previously [26]. Nevertheless, it is advantageous to thermostat the walls, which is particularly important for large pore sizes, high shear rates, and strong fluid–wall interactions.

In this work, the thin fluid layers (less than $0.5\sigma_{ff}$) near the surfaces are thermostated. This is equivalent to thermostating the walls. The Nosé-Hoover thermostat is used to maintain the temperature of the thin fluid layers near the walls at the target value. The equations of motion in the Nosé-Hoover forms are

$$\frac{\mathrm{d}v}{\mathrm{d}t} = -\frac{1}{m}\nabla E - \xi v, \tag{8}$$

with

$$\frac{\mathrm{d}\xi}{\mathrm{d}t} = \frac{1}{\tau^2}\left[\frac{T_0}{T} - 1\right],$$

where τ is the relaxation time of the thermostat. In a fluid under shear flow the velocity of the particles can be divided into two contributions: the contribution due to local stream velocity and the contribution due to thermal motion. A thermostat should act only on the thermal part of the particle velocity. It is difficult to implement the thermostat on the velocity component in the direction of the flow since this is unknown a priori. There are several ways of addressing this problem, for example, by applying the thermostat only on the y and/or z velocity components (we assume that the induced flow moves in the x direction). In this work, the thermostat is applied only on the y and z velocity components. Thus, T_0 in Eq. (8) is calculated from $1/g \sum(mv_{yi}^2 + mv_{zi}^2)$, where g is the number of degrees of freedom. The equation of motion with a constraint force for fixed bond length coupled with the Nosé-Hoover thermostat is integrated using the velocity version of the Verlet algorithm (RATTLE). In this scheme [50], positions and velocities at time t+Δt are given as

$$\begin{aligned} r_i(t+\Delta t) &= r_i(t) + \Delta t v_i(t) \\ &\quad + \frac{\Delta t^2}{2m}[F_i(t) + G_i(t) - m\zeta(t)v_i(t)], \\ v_i(t+\Delta t) &= v_i(t) + \frac{\Delta t}{2m}[F_i(t) + G_i(t) - m\zeta(t)v_i(t)] \\ &\quad + \frac{\Delta t}{2m}[F_i(t+\Delta t) + G_i(t+\Delta t) \\ &\quad - m\zeta(t+\Delta t)v_i(t+\Delta t)], \end{aligned} \tag{9}$$

where G_i is the constraint force on the particles i. An iterative procedure is required to solve the equations [50]. For constant-pressure simulations, an additional damping term is added to the equation of motion [26,52,53]. Most simulations were performed for a total simulation time of 1 ns with a timestep of 4 fs.

3. Results and discussion

In this section, we present constant-volume and constant-pressure MD simulation results for the structure, orientation, velocity profile, and shear viscosity of *n*-decane confined between graphite surfaces at T^*=4.0 (480 K) at several shear velocities. The effect of surface corrugation, wall–fluid strength, and load is investigated. For simulations of confined fluids under shear it usually takes much longer to obtain clean flow fields than density profiles. Thus, one of the best ways to determine if a system has reached steady-state is to monitor the velocity field. Another way is to monitor the values of the shear stress $\langle\tau_{zx}\rangle$ calculated from the friction forces and from the average heat dissipated per unit of time at steady-state. A good test of the accuracy of the simulation is an agreement in the two values of $\langle\tau_{zx}\rangle$.

3.1. *n-decane confined between graphite surfaces under shear*

For hydrocarbon chain molecules, the density and velocity profiles can be obtained based on the center of mass of the molecules or the methylene subunits. The density distribution of the methylene subunits shows more structure than that of the center of mass of the molecules as a whole. The methylene subunits prefer being placed in the proximity of the solid surface. Fig. 2(a) displays the methylene density profile at H^*=8 (2.822 nm), U^*=3.5 (902.5 m/s) and λ=1 in Eq. (7). The density profile was computed by dividing the region between the walls into a number of thin slices with a bin size of 0.035 nm. The time averaged density for each slice is calculated during a simulation by assuming the symmetry of the density profile. Sharp peaks near the surfaces are clearly shown in Fig. 2(a), indicating that the chains tend to wet the surfaces. In the peaks near the surfaces, a maximum and a shoulder appear. This phenomenon has been observed by other workers [25]. The positions of the minimum energy in the site-wall function are different along the direction normal to the wall for an interaction site at different lateral positions over the graphite basal plane as shown in Fig. 1(a). The competition between intra- and inter-molecular spacings leads to different locations of the sites over the unit lattice cell, resulting in a peak and a shoulder in the contact layer. Examination of the density profiles under different shear rates indicates that the density profile is insensitive to the shear velocity. The orientation order parameter of the chains in the pore is given in Fig. 2(b) by assuming the symmetry of the orientation profile across the pore. The order parameter is defined as

$$S=\frac{3\langle\cos^2\theta\rangle-1}{2}, \tag{10}$$

where $\langle\ldots\rangle$ indicates the ensemble average and θ is the angle between the chain-end-to-end vector and the z-axis perpendicular to the wall. By definition, S=−0.5 if molecules lie parallel to the surface and S=0 if molecules are randomly oriented. As shown in Fig. 2(b), the chain molecules in the contact layer lie parallel to the surface while the orientation of the chain molecules is on average random in the interlayer. The center-of-mass velocity profiles for H^*=8 are given in Fig. 3. While the density distribution of the methylene subunits shows more structure than their center-of-mass counterparts, velocity profiles for both the methylene subunits and the center of mass of the molecules are fairly equal. In our simulations, the x components of the velocities for all particles were averaged within bins ($1.0\sigma_{\mathrm{ff}}$ for contact layer, $1.0\sigma_{\mathrm{ff}}$ for second layer and $2.0\sigma_{\mathrm{ff}}$ for inner layer) corresponding to fluid layers determined from density profiles. The hydrodynamics theory predicts a perfect linear velocity profile (u_x^*/U^* versus Z^*) running from −1 to 1. As

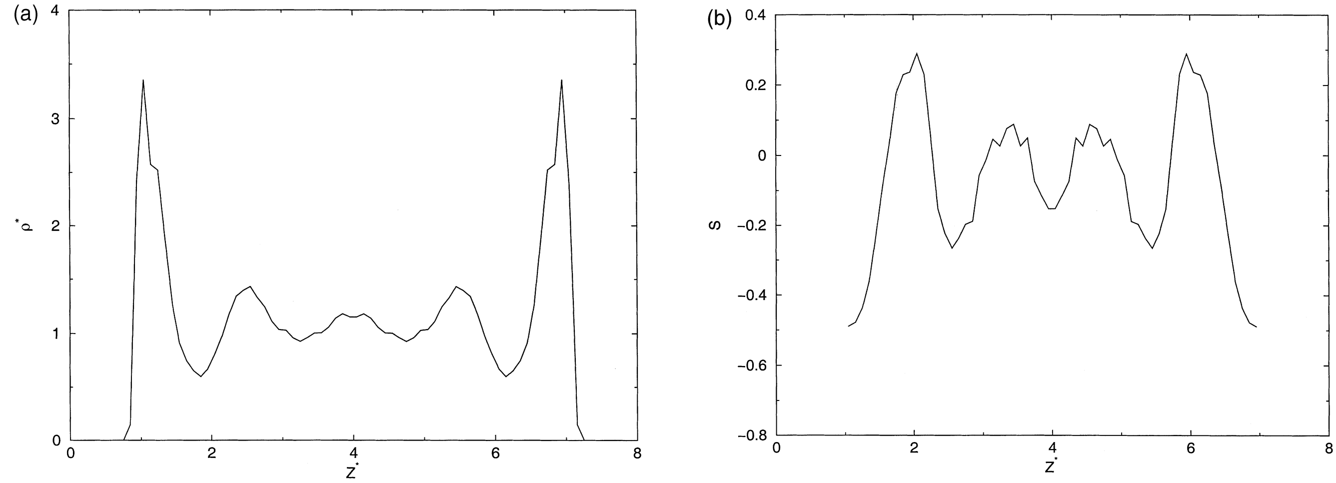

Fig. 2. (a) Methylene density profile of *n*-decane confined between graphite surfaces with λ=1 at T^*=4.0 (480 K), H^*=8 (2.822 nm) and U^*=3.5 (902.5 m/s) from constant-volume MD simulations, and (b) corresponding orientation order parameter profile across the pore.

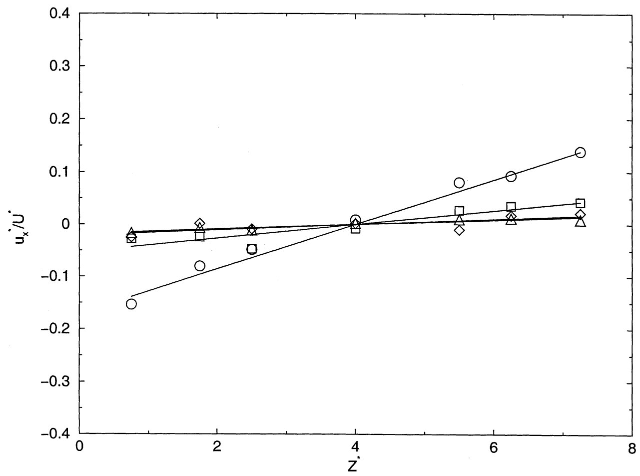

Fig. 3. Velocity profiles of *n*-decane confined between graphite surfaces with λ=1 at T^*=4.0 and H^*=8 from constant-volume MD simulations for various shear velocities – 0.25 (○), 1.0 (□), 2.0 (◇), and 3.5 (△).

shown in Fig. 3, slip always occurs for all cases and the flow is plug-like. In fact, only less than 15% of the shear occurs within the film. As the shear rate increases, the velocity profile deviates more from the perfect linear velocity and the slope decreases. The slopes are 0.043, 0.013, 0.005, and 0.004 for U^*=0.25, 1.0, 2.0, and 3.5, respectively. At the largest shear rate studied, the slope of the profile decreases almost to the point where it is almost flat everywhere in the fluid, indicating a complete decoupling of the fluid and wall motion. The effect of wall–fluid interaction, shear rate, and wall separation on density and velocity profiles has been studied previously in detail for spherical molecules [14,15,38]. It was found that the velocity profile deviates more from the continuum linear form for smaller pore separations (or higher pressures), lower temperatures, and increasing shear rates. The general conclusions for spherical molecules could be applied to chain molecules even though they differ in several ways. For example, the competition between intra- and inter-molecular spacings leads to less pronounced layering with chain molecules. In the SFA experiments [12,40], the effective viscosity (η_{eff}) is calculated from experimental measurements of the shear stress (τ_{zx}) and the applied shear rate (γ), which is determined using the measured plate separation (*H*) and assuming a linear profile between plates,

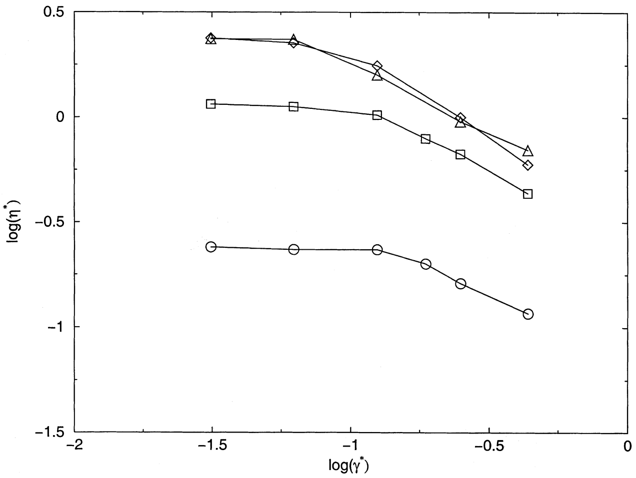

Fig. 4. Effective viscosity versus shear rate curves for (a) *n*-decane confined between graphite surfaces with λ=1 at T^*=4.0 and H^*=8 from constant-volume simulations (○), (b) the same as (a), but with λ=2 (□), (c) the same as (a), but with the graphite energy parameter (ε/k=28) being changed to 1000 K (◇), and (d) the same as (c), but from constant-pressure simulations with P^*=5 (188 MPa) (△).

$$\eta_{\text{eff}} = \frac{\tau_{zx}}{\gamma} = \frac{\tau_{zx}H}{U}. \tag{11}$$

The universal power law observed by Robbins et al. [16,17] is based on the effective viscosity versus shear rate curves. Thus, the effective viscosity is calculated in this work. From the effective viscosity versus shear rate curve shown in Fig. 4, we observe a plateau at low shear rates and shear thinning behavior at high shear rates. If the data in the shear

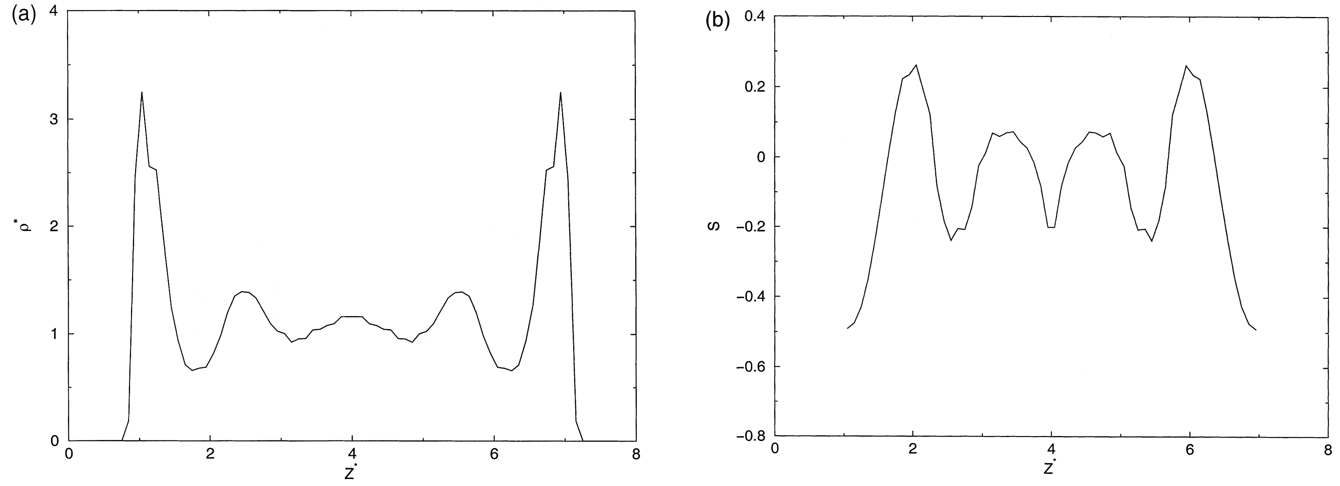

Fig. 5. The same as Fig. 2, but with λ=2.

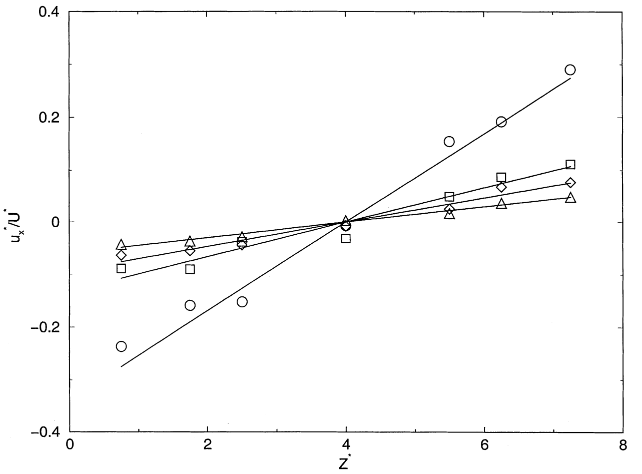

Fig. 6. The same as Fig. 3, but with λ=2.

thinning regime are fitted to the power law, we obtain α=0.56. In a recent work by Wang et al. [39], it was shown that the effective viscosity versus shear rate curve exhibits a shear thinning behavior while the actual viscosity versus shear rate curve shows a basically constant viscosity over the same range of shear rates. As pointed out by these authors [39], the shear thinning reported by some workers may be related to the slip phenomena due to the assumption of the no-slip boundary condition. An increase in surface corrugation, wall–fluid interaction strength and load causes an increase in the effective viscosities as discussed in the next section.

3.2. The effect of surface corrugation

The λ in Eq. (7) is a parameter that enables the corrugation of the wall potential to be varied. The advantage of using the value of λ is that the effect of surface corrugation can be studied without changing the average wall–fluid interaction strength. The methylene density profile at H^*=8 and U^*=3.5 with λ=2 is shown in Fig. 5(a). The density profiles are almost identical for both λ=1 and 2, indicating that an enhancement in surface corrugation does not change the density distribution at the temperature studied. This is consistent with what we found before [54]. Fluid density profiles are insensitive to the detailed structures of the surfaces at high temperatures. The orientation order parameter profile of the chain molecules in the pore is shown in Fig. 5(b). As in Fig. 2(b), the chain molecules in the contact layer lie parallel to the surface while the orientation of the chain molecules is on average random in the interlayer. The velocity profiles for H^*=8 with λ=2 at various shear velocities are given in Fig. 6. As in Fig. 3, the system exhibits plug-like flow and the velocity profiles deviate more from the perfect linear velocity as the shear rate increases, but with slopes larger than their counterparts in the case of λ=1. With the enhancement of surface corrugation which is equivalent to an increase in wall–fluid interaction strength, the coupling between fluid and surface increases. The slopes of the velocity profiles are 0.084, 0.033, 0.023, and 0.015 for U^*=0.25, 1.0, 2.0, and 3.5, respectively. As shown in Fig. 4, the effective viscosity increases by five times as the value of λ increases from 1 to 2. Furthermore, the drop in the viscosity is 0.72 in the case of λ=2, larger than the drop of 0.16 in the case of λ=1 as the shear velocity increases from 0.25 to 3.5. If the data in the shear thinning region are fit to a power law, the exponent α obtained is 0.68. It is interesting to observe that the surface corrugation has a pronounced effect on rheological properties, but not on structural properties.

3.3. The effect of wall–fluid strength

Stevens et al. [37] simulated confined hexadecane fluids using a realistic model and found that the value of α depends on the wall–fluid interaction strength. For weak wall–fluid coupling (ε_w=0.1 kcal/mol), the value of α was found to be 0.05–0.17. They also found increasing viscosity with

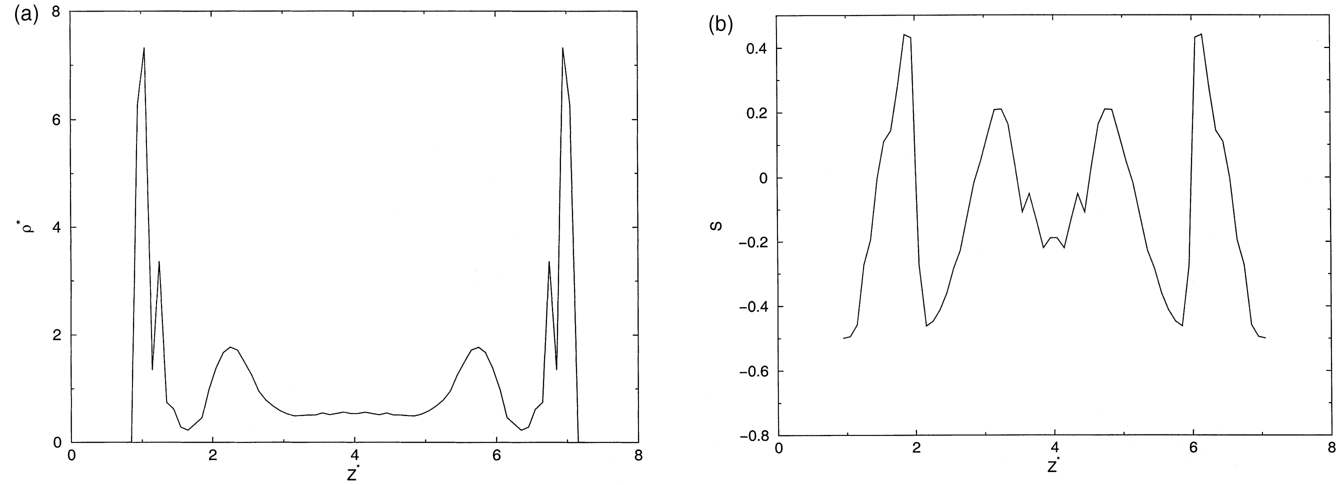

Fig. 7. The same as Fig. 2, but with the graphite energy parameter (ε_{ss}/k=28 K) being changed to 1000 K.

increasing plate separation, in contrast to the experiments [40,41]. As ε_w increases to 0.7 kcal/mol, the value of α was found to be 0.39–0.42. The dependence of α on the wall–fluid interaction strength was also found in other recent simulations [35]. In order to study the effect of wall–fluid interaction strength on the flow BC and shear viscosity, the wall energy parameter ε_{ss}/k is increased from 28 (graphite) to 1000 K. The methylene density profile for H^*=8 and U^*=3.5 is given in Fig. 7(a). There are two distinct layers near the surfaces with density depletion in the center of the pore due to strong wall–fluid interactions. The peak near the surface is significantly higher than with ε_{ss}/k=28 K as shown in Fig. 2(a) and Fig. 5(a). A maximum and a shoulder are observed at the contact layer for the same reason as discussed in Section 3.1. Fig. 7(b) displays the orientation order parameter across the pore. The results are similar to those with ε_{ss}/k=28 K, shown in Fig. 2(b) and Fig. 4(b) except that the second layers also lie parallel to the

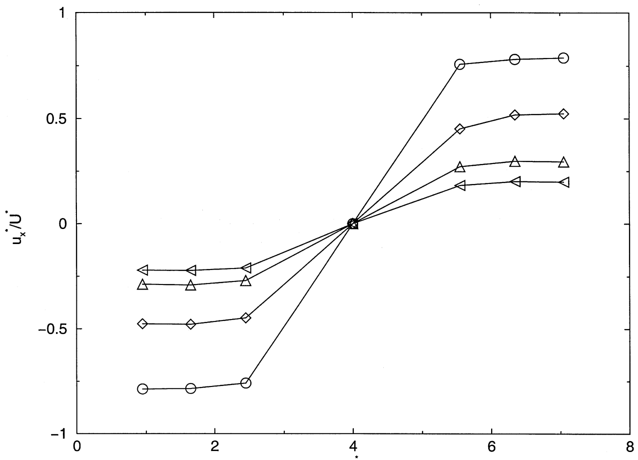

Fig. 8. The same as Fig. 3, but with the graphite energy parameter (ε_{ss}/k=28 K) being changed to 1000 K.

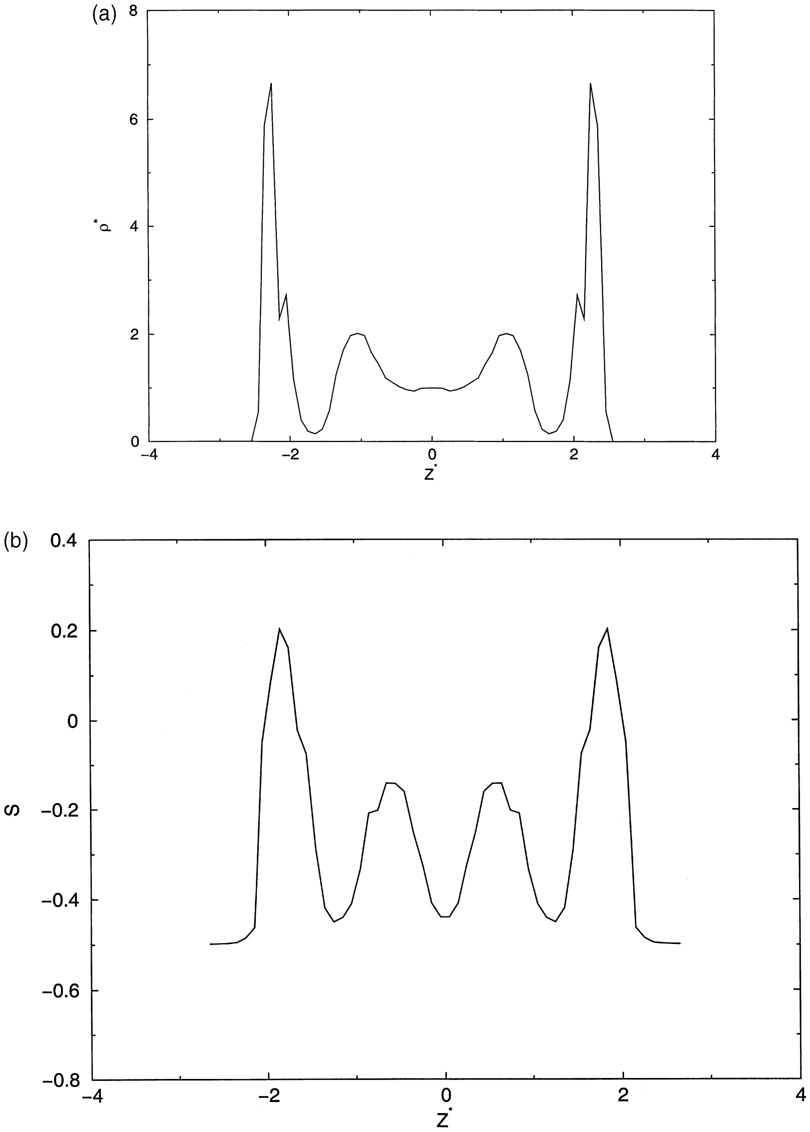

Fig. 9. The same as Fig. 7, but from constant-pressure MD simulations with P^*=5.

surfaces. The velocity profiles are shown in Fig. 8. It is interesting to observe that the fluid layers near the walls are locked to each other while slip occurs at the solid–fluid interface for confined decane. To the best of our knowledge, this is the first observation of this phenomenon. For spherical molecules, locking is always observed when there is no-slip [14,15,38]. This is due to the fact that spherical molecules can easily form commensurate structures on the surface when wall–fluid interactions are strong. For chain molecules, the competition between intra- and inter-molecular spacings makes it difficult for chain molecules to form such commensurate structures on the surface. Thus, slip can still occur even under relatively high wall–fluid interaction strength while commensurate structures are formed between fluid layers. In this case, the contact and the second layers both lie parallel to the surfaces (Fig. 7(b)) and move in a same velocity (Fig. 8). The shear viscosity versus shear rate curve in Fig. 4 exhibits the shear thinning behavior with the exponent α=0.70.

3.4. The effect of normal load

Constant-pressure MD simulations were carried out to study the effect of normal load and pore size. The methylene density profile is shown in Fig. 9(a) at $P^*=5$ (188 MPa), $T^*=4$ and $U^*=3.5$ with the wall energy parameter being changed to $\varepsilon/k=1000$ K. Compared with Fig. 7(a), where $H^*=8$ and $P^*\approx1$, the fluid is confined to a smaller pore size of $H^*\approx6.6$. The orientation order parameter is given in Fig. 9(b). Similar to what is observed for other systems discussed in the previous sections, the chain molecules at the contact layer lie parallel to the surfaces. The viscosity versus shear rate curve in Fig. 4 shows the shear thinning behavior with α=0.64. Previous confined simulations of bead-spring chains found α=2/3 at constant-pressure and 1/2 at constant-volume. In fact, the exponent α is strongly dependent on the viscosities at the lower shear rates in the shear thinning regime. Due to the large uncertainty in the viscosities at the low shear rates and relatively narrow shear rates studied, more work is needed to determine the universality of the power law.

4. Conclusions

Constant-volume and constant-pressure molecular dynamics simulations have been carried out to study the structure, orientation, flow boundary condition, and shear viscosity of *n*-decane confined between graphite surfaces at 480 K under various shear rates using an anisotropic united atom model. The effect of surface corrugation, wall–fluid strength, and load on these properties is also studied. Our results show that the distribution of methylene subunits and the orientation of chain molecules are insensitive to shear velocities at the shear rates studied. The chain molecules near the surfaces form peaks and lie parallel to the surfaces. It is interesting to observe that the surface corrugation has a pronounced effect on rheological properties, but not on structural and orientational properties at the temperature studied. The absolute effective viscosity and the drop in the viscosity increase as the value of λ is increased from 1 to 2. Same phenomena are observed as the wall–fluid interaction strength and load are increased. The shear thinning behavior of confined fluids is observed for all cases at high shear rates studied with the exponent of the power law varying from 0.56 to 0.70 in the case of constant-volume simulations and 0.64 in the case of constant-pressure simulations. Our results also show that the velocity profile deviates more from the perfect linear profile with increasing surface corrugation, wall–fluid interaction strength, shear rate, and normal load. Slip occurs throughout the range of parameters studied. It is also interesting to observe that the fluid layers near the walls could be locked to each other even though slip still occurs at the solid–fluid interface. To the best of our knowledge, this is the first observation of this phenomenon from molecular dynamics simulations.

5. Nomenclature

a_1	graphite lattice parameter (nm)
d	distance between the position of the interaction site and the carbon nucleus (nm)
E	potential energy (kJ/mol)
F	force (N)
f	laterally periodic function
G	bond constraint force (N)
g	degree of freedom
H	pore separation (nm)
k_θ	bond-angle bending force constant (kJ/mol/radian^2)
k	Boltzmann constant (kJ/K)
m	atomic mass (a.m.u)
N	number of molecules
P	pressure (MPa)
R_0	equilibrium bond length (nm)
r	particle position (nm)
r_c	cut-off distance (nm)
S	orientation order parameter
T	temperature (K)
U	wall velocity (m/s)
u	layer flow velocity (m/s)
V_m	torsional potential energy parameter (kJ/mol)
v	particle velocity (m/s)
x,y,z	cartesian coordinates

Greek letters

α	exponent in the power law
γ	shear rate (s^{-1})
Δ	separation between graphite lattice planes
Δt	time step (fs)

ε	Lennard-Jones energy parameter (kJ/mol)
η_{eff}	shear viscosity (Pa s)
θ	angle between the chain-end-to-end vector and the z-axis perpendicular to the wall (rad)
θ_0	equilibrium bond angle (rad)
ξ	the additional degree of freedom associated with the Nosé-Hoover thermostat (s^{-1})
ρ	density ($\mathrm{g/cm^3}$)
σ	Lennard-Jones size parameter (nm)
τ_{zx}	shear stress (MPa)
τ	relaxation time of the Nosé-Hoover thermostat (s)
ϕ	torsion angle (rad)

Operator

∇	gradient

Reduced units

H^*	H/σ
T^*	$T/(\varepsilon/k)$
t^*	$(\varepsilon/m\sigma^2)^{1/2}t$
U^*	$(m/\varepsilon)^{1/2}U$
u^*	$(m/\varepsilon)^{1/2}u$
Z^*	z/σ
γ^*	$(m\sigma^2/\varepsilon)^{1/2}\gamma$
η^*	$(\sigma^4/m\varepsilon)^{1/2}\eta$
ρ^*	$\rho\sigma^3$
τ^*	$(\sigma^3/\varepsilon)\tau$

Acknowledgements

The authors gratefully acknowledge Mark O. Robbins, Yuan-Zhong Hu, Evangelos Manias, James N. Glosli, Arun Yethiraj, Mark J. Stevens, and Paz Padilla for many helpful discussions. This work was supported by the National Science Foundation EPSCoR Program, by the Advanced Manufacturing Institute of the State of Kansas, and by the Lawrence Livermore National Laboratory under the auspices of the US Department of Energy pursuant to the University of California, Lawrence Livermore National Laboratory, Contract No. W-7405-ENG-48.

References

[1] B. Bhushan, J.N. Israelachvili, U. Landman, Nanotribology: friction, wear and lubrication at the atomic scale, Nature 374 (1995) 607.

[2] I.L. Singer, H.M. Pollock (Eds.), Fundamentals of Friction: Macroscopic and Microscopic Processes, Kluwer Academic Publishers, Dordrecht, 1992.

[3] B. Bhushan (Ed.), Handbook of Micro/Nanotribology, CRC Press, Boca Raton, FL, 1995.

[4] J.F. Belak (Ed.), Nanotribology, MRS Bull. May 1993.

[5] S. Jiang, J.F. Belak, Molecular dynamics of thin films under shear, in: P.B. Balbuena, J.M. Seminario (Eds.), Molecular Dynamics: from Classical to Quantum Methods, Elsevier, Amsterdam, 1999.

[6] J.A. Harrison, D.W. Brener, Atomic-scale simulation of tribological and related phenomena, in: B. Bhushan (Ed.), Handbook of Micro/Nanotribology, CRC Press, Boca Raton, FL, 1995, pp. 397.

[7] G.K. Batchelor, An Introduction to Fluid Dynamics, Cambridge University Press, Cambridge, 1967.

[8] J.N. Israelachvili, A.M. Homola, P.M. McGuiggan, Dynamic properties of molecularly thin liquid films, Science 240 (1988) 189.

[9] J. Koplik, J.R. Banavar, J.F. Willemsen, Molecular-dynamics of fluid-flow at solid-surfaces, Phys. Fluids A 1 (1989) 781.

[10] U. Heinbuch, J. Fischer, Liquid flow in pores: slip, no-slip, or multilayer sticking, Phys. Rev. A 40 (1989) 1144.

[11] P.A. Thompson, M.O. Robbins, Simulations of contact-line motion-slip and the dynamic contact-angle, Phys. Rev. Lett. 63 (1989) 766.

[12] S. Granick, Motion and relaxation of confined liquids, 253 (1991) 1374.

[13] J. Krim, E.T. Watts, J. Digel, Slippage of simple liquid-films adsorbed on silver and gold substrates, J. Vac. Sci. Technol. A 8 (1990) 3417.

[14] P.A. Thompson, R.O. Robbins, Shear flow near solids: epitaxial order and flow boundary conditions, Phys. Rev. A 41 (1990) 6830.

[15] P.A. Thompson, R.O. Robbins, Origin of stick-slip motion in boundary lubrication, Science 250 (1990) 792.

[16] P.A. Thompson, M.O. Robbins, G.S. Grest, Structure and shear response in nanometer-thick films, Israel J. Chem. 35 (1995) 93.

[17] P.A. Thompson, G.S. Grest, R.O. Robbins, Phase transitions and universal dynamics in confined films, Phys. Rev. Lett. 68 (1992) 3448.

[18] E.D. Smith, M.O. Robbins, M. Cieplak, Friction on adsorbed monolayers, Phys. Rev. B 54 (1996) 8252.

[19] A.R.C. Baljon, M.O. Robbins, Energy-dissipation during rupture of adhesive bonds, Science 271 (1996) 482.

[20] I. Bitsanis, J.J. Magda, M. Tirrel, H.T. Davis, Molecular dynamics of flow in micropores, J. Chem. Phys. 87 (1987) 1733.

[21] I. Bitsanis, S.A. Somers, H.T. Davis, M. Tirrel, Microscopic dynamics of flow in molecularly narrow pores, J. Chem. Phys. 93 (1990) 3427.

[22] I. Bitsanis, C. Pan, The origin of "glassy" dynamics at solid-oligomer interfaces, J. Chem. Phys. 99 (1993) 5520.

[23] M. Lupkowski, F. van Swol, Ultrathin films under shear, J. Chem. Phys. 95 (1991) 1995.

[24] J.N. Glosli, G.M. McClelland, Molecular dynamics study of sliding friction of ordered organic monolayers, Phys. Rev. Lett. 13 (1993) 1960.

[25] P. Padilla, S. Toxvaerd, Fluid alkanes in confined geometries, J. Chem. Phys. 101 (1994) 1490.

[26] P. Padilla, Chemical structure effects on the equilibrium and under shear properties of thin films in confined geometries: A molecular dynamics simulation, J. Chem. Phys. 103 (1995) 2157.

[27] K.J. Tupper, D.W. Brenner, Molecular dynamics simulations of frictionin self-assembled monolayers, Thin Solid Films 253 (1994) 185.

[28] J. Gao, W.D. Luedtke, U. Landman, Nano-elastohydrodynamics: structure, dynamics, and flow in nonuniform lubricated junctions, Science 270 (1995) 605.

[29] J. Gao, W.D. Luedtke, U. Landman, Structure and solvation forces in confined films: linear and branched alkanes, J. Chem. Phys. 106 (1997) 4309.

[30] G.H. Peters, D.J. Tildesley, Computer simulation of the rheology of grafted chains under shear, Phys. Rev. E 52 (1995) 1882.

[31] Y.C. Kong, D.J. Tildesley, J. Alejandre, The molecular dynamics simulation of boundary-layer lubrication, Mol. Phys. 92 (1997) 7.

[32] C.J. Mundy, S. Balasubramanian, K. Bagchi, J.I. Siepmann, M.L. Klein, Equilibrium and nonequilibrium simulation studies of fluid alkanes in bulk and at interfaces, Faraday Discuss. 104 (1996) 17.

[33] E. Manias, I. Bitsanis, G. Hadziioannou, G. Brinke, On the nature of shear thinning in nanoscopically confined films, Europhys. Lett. 33 (1996) 371.

[34] E. Manias, G. Hadziioannou, G. Brinke, Effect of shear on the desorption of oligomers in nanoscopically confined films, J. Chem. Phys. 101 (1994) 1721.

[35] R. Khare, J. de Pablo, A. Yethiraj, Rheology of confined polymer melts, Macromolecules 29 (1996) 7910.

[36] R. Khare, J. de Pablo, A. Yethiraj, Molecular simulation and continuum mechanics study of simple fluids in non-isothermal planar Couette flows, J. Chem. Phys. 107 (1997) 2589.

[37] M.J. Stevens, M. Mondello, G.S. Grest, S.T. Gui, H.D. Cochran, P.T. Cummings, Comparison of shear flow of hexadecane in a confined geometry and in bulk, J. Chem. Phys. 106 (1997) 7303.

[38] A. Jabbarzadeh, J.D. Atkinson, R.I. Tanner, Rheological properties of thin liquid films by molecular dynamics simulations, J. Non-Newtonian Fluid Mech. 69 (1997) 168.

[39] S.A. Gupta, H.D. Cochran, P.T. Cummings, Nanorheology of liquid alkanes, Fluid Phase Equilibria 150–151 (1998) 125.

[40] H.W. Hu, G.A. Carson, S. Granick, Relaxation-time of confined liquids under shear, Phys. Rev. Lett. 66 (1991) 2758.

[41] G.A. Carson, H.W. Hu, S. Granick, S. Jahanmir, R. Horn, Molecular tribology of fluid lubrication-shear thinning, Tribology Trans. 35 (1992) 405.

[42] S. Jiang, K.E. Gubbins, J.A. Zollweg, Adsorption, isosteric heat and commensurate–incommensurate transition of methane on graphite, Mol. Phys. 80 (1993) 103.

[43] J. Ryckaert, A. Bellemans, Molecular dynamics of liquid alkanes, Discuss. Faraday Soc. 66 (1978) 95.

[44] S. Toxvaerd, Molecular dynamics calculation of the equation of state of alkanes, J. Chem. Phys. 93 (1990) 4290.

[45] P. Padilla, S. Toxvaerd, Structure and dynamical behavior of fluid *n*-alkanes, J. Chem. Phys. 95 (1991) 509.

[46] M.P. Allen, D.J. Tildesley, Computer simulations of liquids, Clarendon Press, Oxford, New York, 1987.

[47] W.A. Steele, The interaction of gases with solid surfaces, Pergamon, Oxford, 1974.

[48] W.A. Steele, The physical interaction of gases with crystalline solids, Surf. Sci. 36 (1973) 317.

[49] R.D. Etters, B. Kuchta, J. Belak, Vacancy-induced melting of N_2 adlayers on graphite, Phys. Rev. Lett. 70 (1993) 826.

[50] C. Pierleoni, J. Ryckaert, On the use of the Nosé-Hoover thermostat in the simulation of dynamic properties of a single chain molecule in solvent, Mol. Phys. 75 (1992) 731.

[51] D.J. Evans, G.P. Morris, Phys. Rev. Lett. 56 (1986) 2172.

[52] W.G. Hoover, Constant-pressure equations of motion, Phys. Rev. A 34 (1986) 2499.

[53] M. Ferrario, Thermodynamic constraints, in: M.P. Allen, D.J. Tildesley (Eds.), Computer Simulation in Chemical Physics, Kluwer Academic Press, Dordrecht, 1993, p. 153.

[54] S. Jiang, C. Rhykerd, K.E. Gubbins, Layering, freezing transitions, capillary condensation and diffusion of methane in slit carbon pores, Mol. Phys. 79 (1993) 373.